Zinc-Ion Doped 7-Layer Aurivillius Compounds ($Bi_{8.75}zn_{0.25}ti_7o_{27}$): Structural, Morphological, and Optical Characterization

Hayet Menasra[1], Karima Bounab[2], Chaima Benbrika[3], Lakhdar Smaili[4], Zelikha Necira[5], Hana Chacha[6]

[1, 4, 6] University of Biskra, BP 145 RP, Biskra 07000, Departement of of Industrial Chemistry, Laboratory of Applied Chemistry(Algeria).

[2, 3, 5] University of Biskra, BP 145 RP, Biskra 07000, Departement of Science of Matter, Laboratory of Applied Chemistry (Algeria).

The Author's Email: h.menasra@univ-biskra.dz[1], karima.bounab@univ-biskra.dz[2], chaima.benbrika@univ-biskra.dz[3], lakhdar.smaili@univ-biskra.dz4, z.necira@univ-biskra.dz[5], hanachacha16@gmail.com[6].

Received: 06/2023 **Published: 09/2023**

Abstract:

In this research, In this study, a novel seven-layer Aurivillius phase, $Bi_{8.75}Zn_{0.25}Ti_7O_{27}$ denoted as BZT, was synthesized using the molten salt method. The investigation included an analysis of its crystal structure, morphology, optical properties, and photocatalytic performance in the degradation of rhodamine-B. X-ray diffraction (XRD) data revealed the adoption of a C-type orthorhombic crystal structure indicated the incorporation of Zn^{2+}/Bi^{3+} ions into the perovskite A-site of Arivillius. Fourier-transform infrared (FTIR) analysis prouve the formation of Ti–O–Ti linkages on the B-site Aurivillius. The calculated band gap energy using the Tauc method was determined to be 2.05 eV, providing evidence of its photocatalytic effects. Additionally, experiments involving the degradation of rhodamine-B under solar irradiation exhibited an efficiency of 67%, offering a compelling demonstration of the material's potential for sustainable and efficient photocatalytic applications.

Keywords: Zinc dopant, layer-Aurivillius, molten salt, photocatalyst.

Tob Regul Sci. ™ 2023 ;9(1) : 5006-5016
DOI : doi.org/10.18001/TRS.9.1.347

1. Introduction

Photocatalysis, the process of initiating chemical reactions under the influence of light, has emerged as a promising technology to address various environmental and energy-related challenges [1-5]. This innovation relies on the meticulous design of efficient photocatalytic materials capable of converting solar light into chemical energy with enhanced efficiency [6, 7]. Among these materials, Aurivillius compounds have captured researchers' interest since their

discovery in 1949, due to their layered crystalline structures defined by the general formula $(Bi_2O_2)^{2+}(A_{n-1}B_{3n}X_{3n+1})^{2-}$. In this formula, "A" typically corresponds to Bismuth, "B" represents transition metal cations, "X" is usually an oxygen anion, and "n" indicates the number of Aurivillius layers[8, 9]. Beyond their remarkable electrical and dielectric properties [10-12], these compounds also stand out for their photocatalytic properties[6, 13, 14].

The Aurivillius structure offers significant flexibility in terms of doping, enabling the introduction of dopant atoms into the "A" and "B" sites of the general formula to enhance dielectric, piezoelectric, and even photocatalytic properties [6, 15].

Zinc ions have demonstrated their significance in improving the photocatalytic properties of various materials, including multilayer Aurivillius structures. Indeed, zinc ions can act as dopants in the "A" or "B" site of the Aurivillius structure due to their ionic radius of 0.74 angstroms. For instance, doping in the "B" site of double-layer Aurivillius compounds such as Bi_2WO_6[16-19], Sr_2AlTaO_6[20], $MnFe_2O_4$[21]…., or in the "A" site of three-layer Aurivillius compounds like $Bi_4Ti_3O_{12}$[22-24] and even four-layer Aurivillius compounds like $Bi_5Ti_3O_{15}$ [25-27] for magnetic and photocatalytic applications. However, the exploration of zinc ion doping in seven-layer Aurivillius compounds remains unexplored, thus offering avenues for original research and investigation.

In this study, our aim is to investigate the impact of 25% zinc ion doping in 7-layer Aurivillius compounds synthesized via the molten salt process, specifically ($Bi_{8.75}Zn_{0.25}Ti_7O_{27}$), for photocatalytic applications. We will examine the structural changes induced by zinc ions using techniques such as X-ray diffraction (XRD) and Fourier-transform infrared spectroscopy (FTIR). Additionally, we will evaluate the optical properties and photocatalytic performance through the degradation of rhodamine-B under solar irradiation.

2. Experimental

2.1. Sample Preparation and characterization

The molten salt method was utilized for synthesizing $Bi_{8.75}Zn_{0.25}Ti_7O_{27}$ (abbreviated as BZT), selected due to its lower operational temperature compared to alternative methods employed in Aurivillius synthesis[28, 29]. Stoichiometric quantities of high-purity precursors, including Bi_2O_3 (99.9%), ZnO (99.8%), and TiO_2 (99.9%), were finely ground along with a 1:1 ratio of (KCl:NaCl) for a duration of 4 hours. Subsequently, the resultant mixture underwent calcination at 850°C for 4 hours, utilizing a gradual heating rate of 2°C/min. The calcined product was meticulously washed with hot water to eliminate any residual chlorine, a process verified by the $AgNO_3$ test.

Following this purification step, the dried material underwent a comprehensive series of analyses. X-ray powder diffraction (XRD) was conducted in the 2θ range of [5°- 70°] using an X-ray powder diffractometer (Rigaku Miniflex 600) with CuKα radiation (λ=1.5406 Å). The raw data were analyzed using the HighScore Plus software. Fourier-transform infrared (FT-IR) spectra were recorded to confirm the crystal phases of the prepared samples. Scanning electron

microscopy (SEM) (TESCAN VEGA3 SEM: Carl Zeiss 300VP) was employed for morphological assessment, accompanied by energy-dispersive X-ray spectroscopy (EDX) for elemental distribution analysis on the same surface. Furthermore, the optical properties of the catalysts within the 400-800 nm range were investigated using a UV-Vis spectrophotometer (Shimadzu FTIR-8400). Additionally, the degradation kinetics of Rh-B under sunlight irradiation were probed using UV-visible spectroscopy.

2.2. Photocatalytic Test

In all photocatalytic activity experiments, BZT catalysts (100 mg) were immersed in a solution of Rhodamine B (Rh-B) dye (100 ml, 10 $mg.l^{-1}$) and subjected to solar irradiation during the month of March in the Biskra region (Algeria). The dye's absorption was analyzed using a UV-vis-NIR spectrophotometer (Perkin-Elmer, Lambda 850) at a wavelength (λ) of 554 nm. At 15-minute intervals of solar exposure, samples (4 mL) of the reaction mixture were extracted, followed by centrifugation (3000 rpm for 10 minutes) and filtration. Subsequently, the filtrates underwent analysis.

The degradation efficiency was determined using the following equation (1):

$$R_{(Rh\text{-}B)}\ (\%) = ((C_0 - C_t)) / C_0 \times 100\ \% \qquad (1)$$

Where; C_0 (mg/l) represents the initial concentration of Rh-B, and C_t (mg/l) is the concentration of the collected samples after centrifugation.

The Fig. 1 illustrate the molten salt stepwise preparation and characterization of BZT photocatalyst.

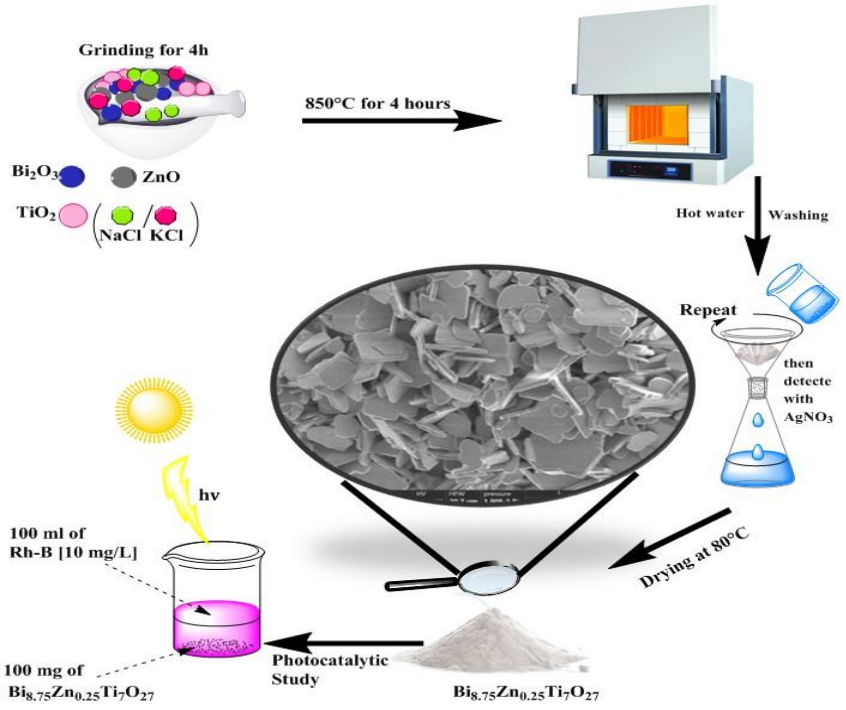

Fig. 1. Molten salt stepwise synthesis and characterization of BZT nano-photocatalyst.

3. Result and Discussion

3.1. XRD analysis

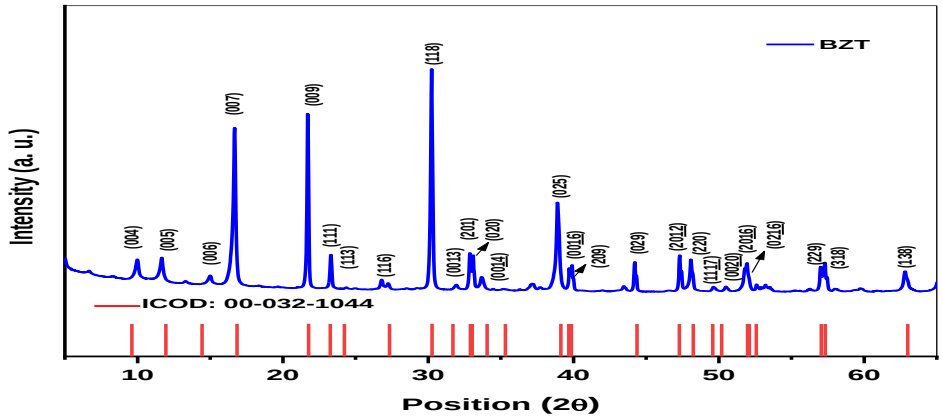

Fig.2. XRD pattern of calcined BZT sample

The X-ray diffraction (XRD) spectrum (Fig. 2) revealed a significant correlation with the seven-layer Aurivillius phase doped with 5% sodium, synthesized through the solid-solid method by UCHIDA et al.[30], identified by the ICOD (No. 00-023-1044). The indexed pattern affirmed the orthorhombic structure within space group C, with lattice parameters calculated using HighScore Plus software (a = 5.451 Å, b = 5.414 Å, c = 35.38 Å, α = β = γ = 90°). Notably, a subtle shift was observed in the peak corresponding to the highest intensity (118), transitioning from an angle of 30.273° to 30.233°. This shift indicates the successful substitution of Bi^{3+} ions (1.03 Å) by Zn^{2+} ions (0.74 Å), confirming effective doping and structural modification within the BZT compound.

Furthermore, the crystallite size was estimated using Debye–Scherer's equation[9], ($D_{sch} = (k \times \lambda)/(\beta\cos(\theta))$, where k= 0.9 is the shape factore and β is the full width at half maximum and $\cos(\theta)$ is the diffraction angle. This calculation was applied to the (118) peak, resulting in an average crystallite size of 664 Å.

3.2.FTIR analysis

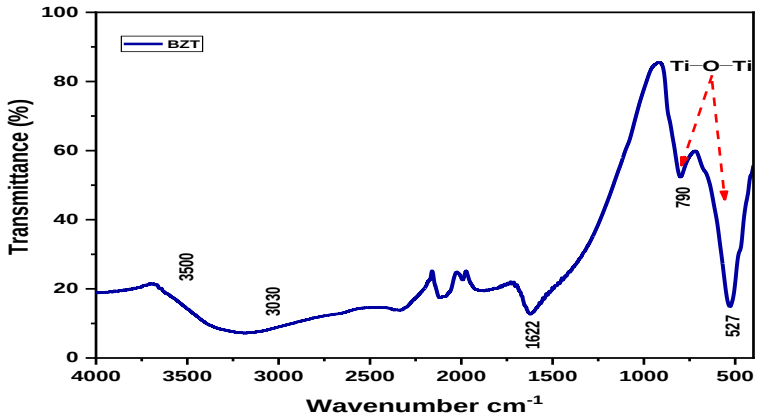

Fig.3. FT- IR absorption spectra of BZTsample calcined at 850°C

Infrared spectroscopy (FTIR) serves as a complementary analysis that provides insights into the formation and stabilization of the phase structure following the doping of the $Bi_9Ti_7O_{27}$ compound. **Fig. 3** illustrates the results of this analysis in the range of 4000-400 cm^{-1}, presenting the spectrum of BZT calcined at 900°C. The bands extending from 790 cm^{-1} to 527 cm^{-1} have been attributed to the antisymmetric stretching vibrations in the Ti–O–Ti linkage of TiO_6[31, 32], representing a regular octahedral configuration characteristic of the seven-Aurivillius phase. These spectral data were consistent with values reported in the literature[32, 33]. Furthermore, the peak at around 1622 cm^{-1} and the broad band within the range of [3500, 3030] cm^{-1} have been attributed to the vibrations of H-O molecules from water absorbed by the KBr, which was used to dilute the samples into pellets[9, 34].

3.3. SEM/ X-EDX analysis

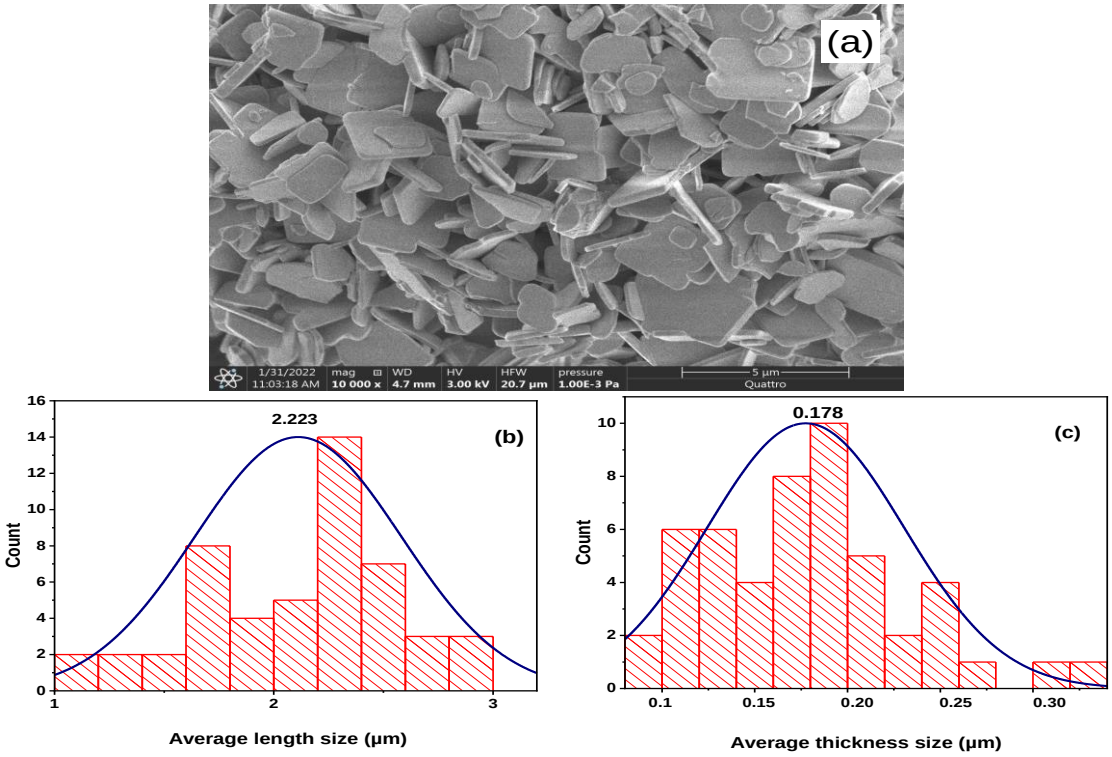

Fig. 4. (a) SEM micrograph of BZT sample calcined at 900 °C, (b, c) Histograms of average length and thickness of BZT plaque-like grains

The observation of SEM micrographs of the BZT material, as illustrated in Fig. 4(a), reveals that the grain morphology takes the form of plates, which is generally attributed to a faster growth rate of grains along the a-b plane compared to the c-axis in materials with a bismuth layer structure[35-37]. Utilizing the 'Image J' software for calculating the average size of the plates yields values of approximately 2.223 µm in length and 0.178 µm in thickness, respectively. We can account for the significant difference in values obtained through the

Debye-Scherrer method (66.4 µm) by considering the agglomeration of crystallites to form plate-like grains[38].
Furthermore, the analysis conducted using energy-dispersive X-ray spectroscopy (EDX), as shown in Fig. 5 has confirmed the purity of the sample prepared through the molten-salt process, evident from the presence of peaks corresponding to all stoichiometric elements, Bi, Ti, Zn, and O.

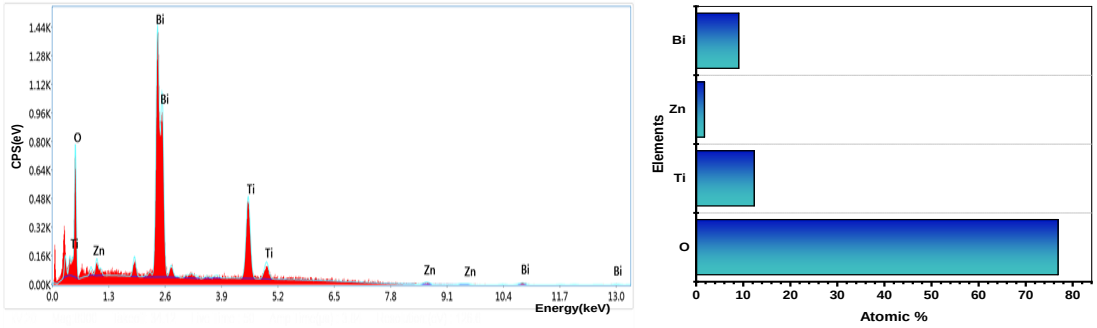

Fig. 5. EDS elements content image of BZT 7-layer Aurivillius nanomaterial

3.4 Optical and Photodegradation Kinetics Study

The discovery of the layer-Aurivillius phase has solidified its reputation as an efficient photocatalyst, mainly attributed to its remarkable capability to rapidly break down and mineralize a diverse range of natural organic materials and pollutants[39-41]. This high efficiency is a result of its narrow bandgap, typically falling within the range of 2.02 to 3.5 eV[39, 42].

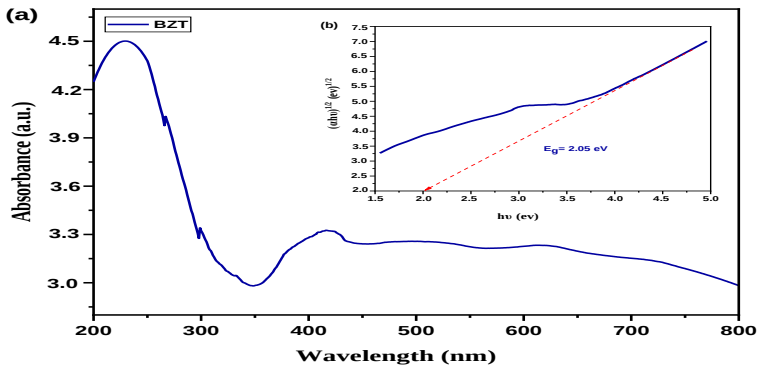

Fig. 6. (a) UV–vis absorbance spectra (b) Fitting (h)$^{1/2}$ vs (h) using Wood and Tauc model for calcined BZT nanomaterial.

The optical bandgap of the calcined BZT nanomaterial at 850°C was determined using the analytical model proposed by Wood and Tauc[43, 44], employing an indirect transition method. Plotting the curve of $(\alpha h\nu)^{1/2}$ against $(h\nu)$ resulted in an estimated bandgap energy of 2.05 eV. Notably, this value is lower than the bandgap of the orthorhombically distorted three and four-layer Aurivillius phases, which were recently reported as 2.25 eV and 3.7 eV, [42, 45]

To assess the photocatalytic capability of the BZT nanomaterial, its efficiency in breaking down Rhodamine-B (Rh-B) pollutants was evaluated. Rhodamine-B, with a peak absorption wavelength of 554 nm in aqueous environments, was chosen as the model pollutant. The finely powdered BZT compound was allowed to reach desorption/adsorption equilibrium during a 30-minute period of darkness before commencing the photocatalytic experiment.

Figure 6(a) illustrates the degradation profiles of Rhodamine-B during exposure to solar irradiation. Remarkably, BZT emerges as an effective catalyst, leading to a substantial 67% reduction in the concentration of Rhodamine-B after a 180-minute irradiation period.

Moreover, the assessment of photodegradation kinetics for various organic molecules typically follows a first-order reaction pattern, consistent with the Langmuir-Hinshelwood kinetic model, especially at lower concentrations[13].

Thus, equation (2) is expressed as:

$$V = -dC/dt = k_{app.} \times C \qquad (2)$$

Where:

V: Rate of photocatalytic degradation ($mg.l^{-1}.min^{-1}$)

$k_{app.}$: Apparent degradation rate constant (min^{-1})

C: Concentration of Rhodamine-B dye in the solution ($mg.l^{-1}$)

t: Duration of irradiation (min)

Integrating equation (2), considering $C = C_0$ when $t = 0$, results in the subsequent equation(3):

$$\ln (C_0/Ct) = k_{app.} \times t \qquad (3)$$

A linear regression analysis of Ln (Ct/C0) against t (Fig. 6(b)) yielded a regression coefficient of 0.98 and a kinetic constant of 0.00277 min^{-1}.

Particularly noteworthy is the presence of extremely reactive ·OH radicals, which emerge near the catalyst's surface. Triggered by the presence of water and atmospheric oxygen, these radicals initiate the partial or complete breakdown of numerous organic compounds through the cleavage of chemical bonds. Due to their transient nature, these radicals exhibit limited diffusion away from the active surface[46, 47].

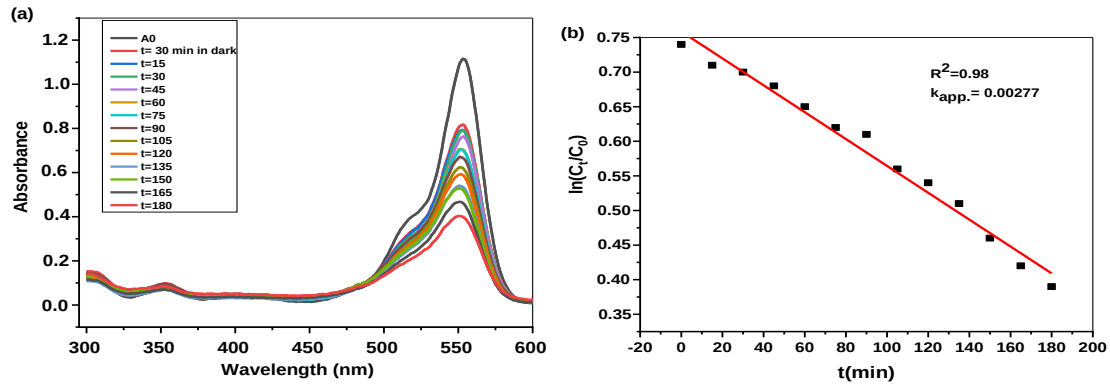

Fig. 7. (a) UV-Vis spectra, and (b) First order kinetic curve for Rhodamine-B (Rh-B) degradation under sunlight irradiation using BZT nanocatalyst

4. Conclusion

In this study, a novel Zn^{2+} doped seven-layer Aurivillius phase, designated as BZT ($Bi_{8.75}Zn_{0.25}Ti_7O_{27}$), was synthesized using the molten salt method. The XRD spectrum analysis confirmed the orthorhombic structure of BZT, while infrared spectroscopy provided complementary evidence of its phase stability, revealing distinct bands associated with Ti–O–Ti linkage vibrations. SEM micrographs unveiled a plate-like grain morphology, measuring 2.223 µm in length and 0.178 µm in thickness. Remarkably, the calculated optical bandgap of the calcined BZT nanomaterial was found to be 2.05 eV, demonstrating a lower value than that reported for orthorhombically distorted layer-Aurivillius phases. Photocatalytic assessment highlighted BZT's effectiveness in degrading Rhodamine-B pollutants, achieving a substantial 67% reduction in concentration after 180 minutes of sunlight irradiation, and exhibiting congruence with first-order reaction kinetics, as indicated by the estimated rate constant (kapp) of 0.00277 min-1. These findings underscore the promising potential of BZT as a photocatalytic agent for environmental remediation purposes.

Acknowledgements

We express our gratitude to **Ms. Soltani Mohamed Toufik** and his engineer, **Sayah Rezgui** from the Laboratory of Photonic Physics and Multifunctional Nanomaterials at Biskra University for their valuable assistance with UV-visible measurements.

References

1. Wu, Q., et al., *The relaxor properties and energy storage performance of Aurivillius compounds with different number of perovskite-like layers.* Journal of Alloys and Compounds, 2022. 911: p. 165081.
2. Hou, D., et al., *Synthesis of porous Bi 4 Ti 3 O 12 nanofibers by electrospinning and their enhanced visible-light-driven photocatalytic properties.* Nanoscale, 2013. 5(5): p. 2028-2035.
3. Ge, W., et al., *Tunable morphology, bandgap, photocatalysis and magnetic properties of Bi6Fe2Ti3O18 nanocrystals by doping cobalt ions.* Journal of Alloys and Compounds, 2019. 799: p. 474-480.
4. Dutta, D.P. and A. Tyagi, *Facile sonochemical synthesis of Ag modified Bi4Ti3O12 nanoparticles with enhanced photocatalytic activity under visible light.* Materials Research Bulletin, 2016. 74: p. 397-407.
5. Hou, D., et al., *Bi 4 Ti 3 O 12 nanofibers–BiOI nanosheets p–n junction: facile synthesis and enhanced visible-light photocatalytic activity.* Nanoscale, 2013. 5(20): p. 9764-9772.
6. Moure, A., *Review and perspectives of aurivillius structures as a lead-free piezoelectric system.* Applied Sciences, 2018. 8(1): p. 62.
7. Gu, Y., et al., *Facile synthesis of sillén-aurivillius layered oxide Bi7Fe2Ti2O17Cl with efficient photocatalytic performance for degradation of tetracycline.* Catalysts, 2022. 12(2): p. 221.

8. Wu, Q., et al., *Design of Lead-Free Films with High Energy Storage Performance via Inserting a Single Perovskite into Bi4Ti3O12**. Chinese Physics Letters, 2020. 37(11): p. 118401.
9. Menasra, H., et al., *Effect of the Synthesis Route on the Structural, Morphological and Dielectric Properties of Bi4 (Ni2/3, Ta1/3) 0.08 Ti2. 92O12 Aurivillius Phases.* Int. J. Thin. Fil. Sci. Tec, 2020. 9(3): p. 181-188.
10. Supriya, S., *Tailoring layered structure of bismuth-based aurivillius perovskites: Recent advances and future aspects.* Coordination Chemistry Reviews, 2023. 479: p. 215010.
11. Peláiz-Barranco, A. and Y. González-Abreu, *Ferroelectric ceramic materials of the Aurivillius family.* Journal of Advanced Dielectrics, 2013. 3(04): p. 1330003.
12. Zuo, X., et al., *Magnetic, dielectric, and magneto-dielectric properties of Aurivillius Bi7Fe2CrTi3O21 ceramic.* Ceramics International, 2018. 44(5): p. 5319-5326.
13. Wang, Y., et al., *Ferroelectric and photocatalytic properties of Aurivillius phase Ca2Bi4Ti5O18.* Journal of the American Ceramic Society, 2021. 104(1): p. 322-328.
14. Ozaki, D., et al., *Synthesis, band structure and photocatalytic properties of Sillén–Aurivillius oxychlorides BaBi 5 Ti 3 O 14 Cl, Ba 2 Bi 5 Ti 4 O 17 Cl and Ba 3 Bi 5 Ti 5 O 20 Cl with triple-, quadruple-and quintuple-perovskite layers.* Journal of Materials Chemistry A, 2021. 9(13): p. 8332-8340.
15. Lomanova, N., *Aurivillius phases Bi m+ 1Fe m–3Ti3O3 m+ 3: Synthesis, structure, and properties (a review).* Russian Journal of Inorganic Chemistry, 2022. 67(6): p. 741-753.
16. Shanthi, S., et al., *Influence of Zn2+ doping on the nonlinear optical limiting characteristics of Bi2WO6 nanostructures for optical device applications.* Materials Chemistry and Physics, 2023. 306: p. 127980.
17. Mandyal, P., et al., *Insight into the properties, morphologies and photocatalytic applications of S-scheme Bi2WO6.* Journal of Environmental Chemical Engineering, 2022. 10(6): p. 108918.
18. Bera, S., et al., *Effect of metal doping in Bi2WO6 micro-flowers for enhanced photoelectrochemical water splitting.* Ceramics International, 2022. 48(23, Part B): p. 35814-35824.
19. Ren, F., J. Zhang, and Y. Wang, *Enhanced photocatalytic activities of Bi 2 WO 6 by introducing Zn to replace Bi lattice sites: a first-principles study.* Rsc Advances, 2015. 5(37): p. 29058-29065.
20. Li, Y.D., et al., *First-principles study on ferromagnetism in double perovskite Sr2AlTaO6 doped with Cu or Zn at B sites.* Physica B: Condensed Matter, 2018. 537: p. 134-138.
21. Manohar, A., et al., *Zn- doped MnFe2O4 nanoparticles for magnetic hyperthermia and their cytotoxicity study in normal and cancer cell lines.* Colloids and Surfaces A: Physicochemical and Engineering Aspects, 2023. 675: p. 132037.
22. Zhou, Q., et al., *In-situ constructed 2D/2D ZnIn2S4/Bi4Ti3O12 S-scheme heterojunction for degradation of tetracycline: Performance and mechanism insights.* Journal of Hazardous Materials, 2022. 438: p. 129438.
23. Belik, A.A., *Rise of A-site columnar-ordered A 2 A′ A″ B 4 O 12 quadruple perovskites with intrinsic triple order.* Dalton Transactions, 2018. 47(10): p. 3209-3217.

24. Zhao, Y., et al., *Enhanced electromechanical properties and conduction behaviors of Aurivillius Bi4Ti2. 95 (B1/3Nb2/3) 0.05 O12 (B= Mg, Zn, Cu) ceramics.* Materials Letters, 2016. 174: p. 242-245.
25. Jabeen, N., et al., *Boosting of Magnetic, Ferroelectric, Energy Storage Efficiency, and Piezoelectric Properties of Zn Intercalated SrBi4Ti4O15-Based Ceramics.* Materials, 2022. 15(14): p. 5057.
26. Sharma, V.K., et al., *Enhanced photocatalytic properties in metal modified bismuth layered ferroelectric ceramics, srbi4ti4o15.* Srbi4ti4o15, 2022.
27. Xi, J., et al., *Preparation and characterization of Zn-modified CaBi 4 Ti 4 O 15 piezoelectric ceramics with lower sintering temperature.* Journal of Materials Science: Materials in Electronics, 2020. 31: p. 8805-8814.
28. Worrall, A., et al., *Molten salt reactors and associated safeguards challenges and opportunities.* 2018.
29. Gupta, S.K. and Y. Mao, *A review on molten salt synthesis of metal oxide nanomaterials: Status, opportunity, and challenge.* Progress in Materials Science, 2021. 117: p. 100734.
30. UCHIDA, K. and T. KIKUCHI, *Subsolidus phase equilibria in the system Na2O-Bi2O3-TiO2 at 1000° C.* Journal of the American Ceramic Society, 1978. 61(1-2): p. 5-8.
31. Bokolia, R., et al., *Dielectric, ferroelectric and photoluminescence properties of Er3+ doped Bi4Ti3O12 ferroelectric ceramics.* Ceramics International, 2015. 41(4): p. 6055-6066.
32. Yokoi, A. and J. Sugishita, *Ferroelectric properties of mixed bismuth layer-structured Na0. 5Bi8. 5Ti7O27 ceramic and SrxNa0. 5− x/2Bi8. 5− x/2Ti7O27 solid solutions.* Journal of Alloys and Compounds, 2008. 452(2): p. 467-472.
33. Wei, T., et al., *Upconversion luminescence and ferroelectric properties of Er3+ doped Bi4Ti3O12–SrBi4Ti4O15.* Materials Letters, 2014. 118: p. 92-95.
34. Cheng, F., et al., *FTIR analysis of water structure and its influence on the flotation of arcanite (K2SO4) and epsomite (MgSO4· 7H2O).* International Journal of Mineral Processing, 2013. 122: p. 36-42.
35. Yan, H., et al., *The effect of (Li,Ce) and (K,Ce) doping in Aurivillius phase material CaBi4Ti4O15.* Materials Research Bulletin, 2004. 39(9): p. 1237-1246.
36. Zhao, W., et al., *Topochemical Synthesis of Plate-Like Na0.5Bi0.5TiO3 from Aurivillius Precursor.* Journal of the American Ceramic Society, 2008. 91(4): p. 1322-1325.
37. Jiang, Y., et al., *Photoluminescence and electrical properties of Er 3+-doped Na 0.5 Bi 4.5 Ti 4 O 15—Bi 4 Ti 3 O 12 inter-growth ferroelectric ceramics.* Frontiers of Materials Science, 2017. 11: p. 51-58.
38. Köseoğlu, Y., et al., *Structural, Conductivity, and Dielectric Properties of Co0.5Mg0.5La0.1Fe1.9O4 Ferrite Nanoparticles.* Journal of Superconductivity and Novel Magnetism, 2016. 29(11): p. 2813-2819.
39. Wang, D., et al., *Synthesis, crystal structure, and photocatalytic activity of the new three-layer aurivillius phases, Bi2ASrTi2TaO12 (A=Bi, La).* Journal of Solid State Chemistry, 2010. 183(2): p. 361-366.

40. Malik, J., S. Kumar, and T.K. Mandal, *Reactive species specific RhB assisted collective photocatalytic degradation of tetracycline antibiotics with triple-layer Aurivillius perovskites.* Catalysis Science & Technology, 2022. 12(22): p. 6704-6716.
41. Rani, S., G. Naresh, and T.K. Mandal, *Coupled-substituted double-layer Aurivillius niobates: structures, magnetism and solar photocatalysis.* Dalton Transactions, 2020. 49(5): p. 1433-1445.
42. Naresh, G. and T.K. Mandal, *Efficient COD Removal Coinciding with Dye Decoloration by Five-Layer Aurivillius Perovskites under Sunlight-Irradiation.* ACS Sustainable Chemistry & Engineering, 2015. 3(11): p. 2900-2908.
43. Shu, Y., et al., *Bandgap tunability of Aurivillius Bi4NdTi3(Fe0.5M0.5)O15 (M=Cr, Ni, Fe, Co, Mn) thin films.* Journal of Alloys and Compounds, 2019. 773: p. 934-939.
44. Ding, Z.Z., et al., *Tuning the band gaps of ferroelectric Aurivillius compounds by transition metal substitution.* Ceramics International, 2020. 46(6): p. 8314-8319.
45. Roselin, A.A., et al., *Bismuth titanate (Bi4Ti3O12, BTO) sol–gel spin coated thin film for heavy metal ion detection.* Journal of Materials Science: Materials in Electronics, 2021. 32(20): p. 24801-24811.
46. Ohtani, B., *Photocatalysis A to Z—What we know and what we do not know in a scientific sense.* Journal of Photochemistry and Photobiology C: Photochemistry Reviews, 2010. 11(4): p. 157-178.
47. Shetty, M., et al., *Photocatalytic Efficiency of Bi-Based Aurivillius Compounds: Critical Review and Discernment of the Factors Involved.* Nanostructured Materials for Environmental Applications, 2021: p. 137-165.